

Fast and Accurate RFIC Performance Prediction via Pin-Level Graph Neural Networks and Probabilistic Flows

Anahita Asadi

*Electrical and Computer Engineering
University of Illinois Chicago
Chicago, Illinois
aasadi5@uic.edu*

Leonid Popryho

*Electrical and Computer Engineering
University of Illinois Chicago
Chicago, Illinois
lpopry2@uic.edu*

Inna Partin-Vaisband

*Electrical and Computer Engineering
University of Illinois Chicago
Chicago, Illinois
vaisband@uic.edu*

Abstract—Accurately predicting the performance of active radio frequency (RF) circuits is essential for modern wireless systems but remains challenging due to highly nonlinear, layout-sensitive behavior and the high computational cost of traditional simulation tools. Existing machine learning (ML) surrogates often require large datasets to generalize across various topologies or to accurately model skewed and multi-modal performance metrics. In this work, a lightweight, data-efficient, and topology-aware graph neural network (GNN) model is proposed for predicting key performance metrics of multiple topologies of active RF circuits such as low noise amplifiers (LNAs), mixers, voltage-controlled oscillators (VCOs), and PAs. To capture transistor-level symmetry and preserve fine-grained connectivity details, circuits are modeled at the device-terminal level, enabling scalable message passing while reducing data requirements. Masked autoregressive flow (MAF) output heads are incorporated to improve robustness in modeling complex target distributions. Experiments on datasets demonstrate high prediction accuracy, with symmetric mean absolute percentage error (sMAPE) and mean relative error (MRE) averaging 2.40% and 2.91%, respectively. Owing to the pin-level conversion of circuit to graph and ML architecture robust to modeling complex densities of RF metrics, the MRE is improved by $3.14\times$ while using $2.24\times$ fewer training samples compared to prior work, demonstrating the method’s effectiveness for rapid and accurate RF circuit design automation.

Index Terms—Graph neural network (GNN), RF circuit modeling, masked autoregressive flow (MAF), electronic design automation (EDA), machine learning.

I. INTRODUCTION

With the growing importance of modern wireless systems (e.g., the Internet of Things [1], 5G [2] RADAR [3], and LiDAR [4]) accurate modeling and optimization of RF integrated circuits (RFICs) is more critical than ever. The performance of key building blocks of such systems, ranging from power amplifiers (PA) to transmitters, directly affects the fidelity, efficiency, and robustness of modern systems. However, their

This work was supported in part by the CogniSense: Center on Cognitive Multi-spectral Sensors, one of seven centers in Joint University Microelectronics Program (JUMP) 2.0, a Semiconductor Research Corporation (SRC) program sponsored by the Defense Advance Research Project Agency (DARPA).

operation in highly nonlinear and layout-sensitive regimes makes accurate modeling particularly challenging.

While highly accurate, traditional simulators (e.g., SPICE, ADS, ANSYS) are computationally expensive, especially when sweeping process-voltage-temperature (PVT) corners or performing extensive design-space exploration. Existing circuit simulators rely on computationally intensive numerical methods, such as trapezoidal, Gear integration, and Newton-Raphson methods [5] while electromagnetic (EM) simulations typically use finite element method (FEM) analysis. Both approaches scale poorly with advancing technologies, particularly when accounting for heterogeneous integration and packaging effects [6]. Substantial expert effort is therefore required to design advanced analog and RF circuits, including topology selection and device sizing, highlighting the need for accurate and fast automation methods.

A broad spectrum of deterministic and ML-based heuristics has been explored in the area of RFIC optimization. Simple local-search heuristics, such as direct binary search (DBS), have been used in [7] for a dual-band filter. In this work, layout is turned into a binary matrix, the bits of which are flipped to improve a given figure of merit (FoM) in a few hundred EM evaluations. However, changing every bit is a greedy strategy prone to getting trapped in FoM local optima. Moreover, mm-Wave designs, requiring finer pixel grids, larger matrices, or tighter control over stop-band roll-off, make this solution inefficient. To escape such issues, meta-heuristic optimizers such as evolutionary algorithms (EAs) [8], [9] and Bayesian optimization (BO) [10] have been proposed. These methods explore rugged, multimodal design spaces requiring gradient information, and are effective with even modest dataset sizes. In higher dimensional RF problems, however, EAs become sample-inefficient and exhibit poor reproducibility due to the stochastic variability across optimization runs until convergence. BO also struggles to scale, as kernel matrix inversion (required for Gaussian process updates) and acquisition function maximization (used to select the next query point) become computationally expensive in high-dimensional spaces, typically beyond a few dozen dimensions, leading to

long run-times and premature convergence. Hence, search-only methods do not scale well to the strongly nonlinear, multi-objective design spaces encountered in practical RF circuits [11].

An alternative strategy is to learn a surrogate model for fast prediction of circuit FoMs and integrate it into the optimization process. Classical deterministic surrogates, such as partial least-squares (PLS) regression [12], perform well when the response surface is nearly linear but lack the expressiveness to capture the strong nonlinearities, outliers, and complex FoM distributions inherent in RFICs. That is, because every component in such models is a weighted combination of all inputs, irrelevant and noisy variables influence and degrade the quality of PLS models. This, in turn, requires manual feature-engineering with reduced number of components, limiting the model's ability to capture complex patterns. On the other hand, ML methods can sidestep these issues by leveraging intrinsically nonlinear models, flexible hyperparameter spaces, built-in robustness to noise and outliers, and GPU acceleration, making them well-suited for a broader range of modeling tasks.

Traditional machine learning (ML) regressors, such as k -nearest neighbors (kNNs), random forests, and support vector regressors (SVRs), have been used for inferring circuit parameters that produce a desired output or performance (i.e., inverse design). Some of these methods achieve mean relative errors (MRE) as low as 0.23% for receiver components consisting of voltage amplifiers (VA), LNAs, and mixers, at a single frequency [13]. However, these approaches are typically limited to linear circuits. For example, in [13], errors rise to $\sim 50\%$ in nonlinear power amplifiers (PAs). In contrast, neural surrogates equipped with techniques such as Monte Carlo dropout or deep ensembles can capture complex nonlinear interactions and provide calibrated uncertainty, making them more suitable for generalizable modeling and downstream optimization.

As a result, a growing body of work has applied neural networks (NNs) in RF domains to model various FoMs from sizing parameters or perform inverse design by predicting parameter sets that meet specified performance targets [14]. One of the simplest NN architectures, feed-forward or artificial neural networks (ANNs), has been widely used for modeling passive RF circuits, including the S-parameters of high-speed links [15] and multilayer interconnects [16]. For more complex circuits with nonlinear active components, such as PAs, both local and global interactions play an important role in circuit behavior. To capture the localized interactions of nonlinear RF components, convolution neural networks (CNNs) should be considered.

As an example, in [17], the S-parameters of a post-layout matching circuit for a PA are modeled and the circuit layout is generated using a genetic algorithm (GA) as the generator and a CNN as the verifier of the insertion loss S-parameter, S_{21} . By optimizing a loss function that simultaneously minimizes the mismatch between the actual and optimal impedance and maximizes S_{21} , the approach achieves approximately $4,500\times$

speedup in the inverse design process. While these algorithms accelerate modeling and optimization for a given circuit, they generalize only to circuits within the same distribution the CNN was trained on. New circuits exhibiting significantly different physics, such as active components or complex FoM distributions, often require exhaustive retraining or entirely new ML model or loss functions, potentially offsetting the benefits of automation. In the same work, transfer learning (TL) is applied to reduce the time required for synthetic dataset generation by leveraging knowledge learned from EM structures in air (i.e., without the complexity introduced by packaging materials, substrate layers, or nearby active components) and transferring it to full-chip dielectric simulations. While presenting a powerful end-to-end circuit design framework, this work still requires a large dataset (over 300,000 simulations) and substantial computational and memory resources.

CNNs integrated with recurrent neural networks (RNNs) are also utilized to capture time-varying nonlinearities. Earlier works use feed-forward ANNs. For example, AM/AM and AM/PM distortion in a Doherty PA are modeled in [18]. However, feed-forward ANNs process each input independently and statically, which limits their generalization to memory effects like thermal or bias-induced distortions. Thus, memory effects are neglected in these static networks. To address this, [19] introduces a deep gated recurrent unit (GRU)-based macromodel regularized with Gaussian dropout. This approach improves generalization to complex output waveforms by combining the compact gating structure of GRUs. GRUs have fewer parameters than other sequence models by better resisting vanishing gradients due to the regularization benefits of Gaussian dropout. The results show that each aforementioned architectural enhancement (whether memory gates, dropout regularization, or bidirectional and high-order networks) consistently yields a double-digit error reduction. By incorporating both bidirectional recurrence and high-order temporal dependencies, recent deep GRU-based variants, such as bidirectional high-order deep RNNs in [20], achieve up to 27% lower test error than standard RNNs when modeling more complex circuits such as amplifiers, voltage-controlled delay lines, and interconnects. Long short-term memory (LSTM)-based macromodels have also been proposed to capture cumulative, time-dependent correlations and nonlinearities in wideband and dynamic RF systems. These models are trained on uniformly distributed noise signals and have demonstrated strong generalization to previously unseen inputs, including sine and dual-tone waveforms, with a low normalized mean square error (NMSE) [21].

Another application of LSTMs is shown in [22], where convolutional encoder-decoder network is incorporated to learn from layout samples with reduced dimensionality and accurately predict broadband S-parameters of two-port passive structures. The model leverages translational invariance (i.e., the ability to recognize recurring layout patterns such as vias, stubs, and interconnects) as well as spatial locality, enabling it to generalize effectively across various layouts, including multi-stub filters, stepped impedance filters, and

radial stubs. This results in inference speeds that are orders-of-magnitude faster than those of EM solvers. Similarly, [23] presents a convolutional autoencoder (AE) that learns a latent space of band-pass filter layouts, in which a separate regressor is trained to predict S-parameters. By pretraining the autoencoder in an unsupervised manner and fine-tuning only the regression head, the approach reduces labeled data requirements by $\sim 85\%$ while maintaining prediction error below $< 1\%$. For integrated voltage regulators, [24] shows the effectiveness of spectral convolutional architectures. In that work, the frequency-domain output is treated as a structured object, and a spectral transposed CNN is employed to map design parameters directly to multi-objective performance metrics, significantly reducing model size while achieving Pareto-optimal trade-offs across power, ripple, and area.

Enforcing physical consistency within learning-based models is another primary concern. While existing NN-based approaches achieve high accuracy in modeling S-parameters, they often fail to satisfy fundamental physical laws, such as causality (e.g., ensuring responses not preceding excitation) and passivity (e.g., guaranteeing the system does not generate energy). This lack of physical consistency can lead to non-physical predictions, which is particularly problematic when the models are used in time-domain simulations or cascaded with other components. To address this, [25] introduces two custom NN layers, one of which enforces consistency with the Kramers–Kronig relations (fundamental causal constraints that link the real and imaginary parts of a system’s frequency) by reconstructing the imaginary part from the real part via Hilbert transform, thereby enforcing time-domain causality. The other layer enforces passivity by constraining the maximum singular value of the S-parameter matrix to remain below 1 across all frequencies, using a differentiable minimum-phase filter constructed during training. Alternatively, physical constraints can be directly embedded into the surrogate model, delegating synthesis to an outer optimization loop. With this approach, the surrogate focuses on fast performance evaluation, while the design task itself is handled by a separate optimizer exploring the parameter space. This is exemplified in [26] where a causality-aware, physics-augmented 3D-to-2D UNet CNN surrogate, trained on only $\sim 4,000$ Ansys HFSS simulations, is combined with a tree-structured Parzen estimator (a BO method) to design low-loss 6-port impedance-transforming networks. The surrogate replaces computationally expensive EM simulations, while the Bayesian optimizer efficiently explores a 28-parameter multilayer design space. In benchmarks, the synthesized layouts outperforms expert-designed counterparts, while reducing design time by orders of magnitude.

Recent work has also explored reinforcement learning (RL) as an unsupervised approach to RF circuit design. For example, [27] uses RL to guide architecture selection and sizing of PAs. However, RL methods typically require extensive simulations, making them less suitable for large-scale systems. Generation of a 35,000 dataset in [27] required ~ 3.3 days on a 192-core cluster. The RL policy is a 2-layer MLP that chooses the PA cell architecture (common-emitter, common-base, and

stack) and sizing parameters and outputs the distribution over design actions. However, these approaches require substantial retraining or adaptation for other circuits, such as VCOs, whether through data-intensive retraining, transfer learning, redesigned physics-informed reward functions, or graph-based augmentations. Thus, despite their early promise, RL-based methods, like other ML approaches, face significant limitations. In particular, they require retraining or adaptation for unseen topologies, as most models are inherently topology-agnostic. Even methods that incorporate topology selection into their search space (e.g., [27]) incur substantial computational cost to support such generalization.

A way to circumvent topology-awareness is to characterize circuits, such as in [28], where modular analysis of passive electrical networks (E-networks) is purposed with fully-connected neural networks, achieving an average R^2 of 95% on some RF circuits with an $\sim 11\times$ reduction in training data. However, the approach struggles to generalize to highly nonlinear circuits like mixers and PAs, whose behavior depends on input power level, biasing conditions, frequency, and internal state—factors not captured by S-parameters at the fundamental frequency. Moreover, changing the number of E-networks and their ports requires retraining of the network, highlighting the importance of considering topology.

To address the issue of generalization, graph neural networks (GNNs) have emerged as a promising modeling approach that naturally captures circuit topology—an important step toward reducing or eliminating the need for retraining when adapting to new circuit designs. By representing nets, components, or terminals as graph nodes, GNNs propagate local operating-point information through message-passing layers, effectively mirroring Kirchhoff’s laws. Early electronic design automation (EDA) research has shown promising results in modeling small-signal analog blocks and RF passive circuits using spatial variants of graph convolutional networks (GCNs) [29]–[33]. Zero- or few-shot methods, which require no retraining or only minimal fine-tuning or transfer learning, have further improved generalization across technologies, variations, and FoMs, highlighting the potential of GNNs to generalize beyond a single circuit topology [32]–[35]. GNNs have also proven effective for post-layout simulation of analog blocks [36]–[38]. The only GNN-based study focused on RF circuits to date, [39], extended this approach to LNAs, mixers, VCOs, and PAs, achieving $R^2 > 80\%$ across FoMs training on a dataset of about 36,000 circuits. However, the graph representation used in [39] obscures component symmetry, posing challenges for integration with frameworks that support subcircuit identification, such as [40], [41]—an essential step for parallelizing time-consuming simulations of large-scale circuits. Moreover, existing GNN surrogates struggle with strongly nonlinear, skewed, or multi-modal distributions governing RF FoMs, such as phase noise and tuning range in VCOs. Thus, more expressive graph models are needed to capture RF circuit behavior with reduced data requirements.

While the aforementioned approaches offer valuable EDA capabilities, each exhibits specific limitations that constrain

their broader applicability to RFIC design. These include high data and compute requirements, limited generalization to new topologies, lack of physical consistency (e.g., causality and passivity), poor scalability to large or irregular circuits, and the need for manual adaptation such as retraining, reward redesign, or topology-specific augmentation. Consequently, the problem remains open, motivating continued exploration of more generalizable and topology-aware solutions. To address this challenge, the following is proposed:

- **Topology-aware GNN for active RF performance prediction.** A graph-based surrogate model tailored to active RF blocks, offering improved data efficiency and accuracy over prior work [39], [42]. RFICs introduce added complexity from high-frequency effects (e.g., mutual coupling) and non-Gaussian FoM distributions, beyond typical analog circuit challenges.
- **Pin-level embedding for scalable evaluation.** Leveraging proposed embeddings, the model captures fine-grain subcircuits, enabling scalable learning and effective RF primitive identification beyond net-based methods.
- **Unified ML architecture for scalar and distributional prediction.** The proposed GNN integrates distinct deterministic and probabilistic output heads to jointly model scalar metrics and complex performance distributions. In particular, the proposed masked autoregressive flow (MAF) output heads accurately capture and generalize over highly nonlinear, skewed, and multi-modal targets.
- **Data-efficient training for competitive accuracy.** The proposed approach achieves an average sMAPE of 2.40% while reducing simulation requirements by $2.24\times$ compared to state-of-the-art, highlighting its practicality in resource-constrained RF design flows.
- **Full GPU-parallelized training and inference for accelerated evaluation.** Unlike traditional CPU-bound simulators (e.g., SPICE), the framework supports full GPU acceleration, achieving speedups of $\sim 5,563\times$ on CPU and $\sim 41,707\times$ on GPU over Spectre for inference tasks.

The remainder of this paper is organized as follows. Recent advances in GNN-assisted RF circuit modeling are reviewed in Section II, with an emphasis on task focus and abstraction level. The proposed GNN-based framework, including graph representations and model architecture, is detailed in Section III. The experimental setup is described in Section IV, and results with comparative analyses are presented in Section V. Conclusions and directions for future work are provided in section VI.

II. GNNs IN EDA: BACKGROUND AND RELATED WORK

GNNs are a class of deep learning models specifically designed to operate on graph-structured data and handle their non-Euclidean nature by learning node, edge, or graph-level representations via message passing mechanisms. Each node’s representation is updated by aggregating transformed features from its neighbors, capturing both local and global graph structures. In their earliest form, recurrent GNNs propagate information iteratively across the graph until convergence,

but incur high memory and computational cost. Algorithms such as gated GNNs were developed to address scalability issues by using GRUs to limit message propagation to a fixed number of steps [44]. Multi-layer perceptron (MLP) with LeakyReLU is used to model S-parameters of circuits with up to six resonators with a significant accuracy degradation in unseen circuits [29]. Spectral GCNs define convolution operations in the spectral (frequency) domain (i.e., using eigen-decomposition of the graph Laplacian) enable more expressive filtering and improved discrimination of graph-level structural and feature patterns. Spatial methods, such as graph isomorphism networks, are used in [33], [45] to capture transistor-level topology features of four operational-amplifier variants and transfer them in zero- and few-shot settings for performance prediction. GraphSAGE, which employs one- and two-hop neighborhood sampling, offers injective aggregation schemes that preserve the uniqueness of node neighborhoods. Nevertheless, compared to spectral GCNs, spatial methods offer lower computational cost, broader applicability to various graph types, including directed graphs, and greater flexibility for inductive learning on entirely new graphs or unseen nodes. These advantages have contributed to their rapid adoption in AI-assisted analog EDA domain. An example of this class is the graph attention network (GAT), which employs masked self-attentional layers to assign different weights to neighboring nodes, enabling more nuanced and context-aware feature aggregation. While the effectiveness of GAT layers has been demonstrated (e.g., in evaluating transistor degradation and threshold voltage shifts in digital circuits [46]), they are found to be less competitive than GCNs for analog and RF circuit modeling. GCNs, on the other hand, have shown promise in several EDA tasks. For example, [30] applies GCNs in combination with RL for transistor sizing optimization. However, as the network depth increases, GCNs tend to suffer from vanishing gradients, over-smoothing, and overfitting, leading to degraded performance. To stabilize the learning process of deep GCNs, pre-activation of residual connections and message normalization allow models such as generalized graph convolution (GENConv) layers [31] to unify message aggregation operations and enable task-specific tuning. In [32], GENConvs are combined with TL to transfer knowledge from DC voltage prediction to AC output voltage and gain prediction via node-level regression, thereby reducing the required dataset size. TL has demonstrated up to $10\times$ data reduction in tasks such as GNN generalization across different technologies [30], [34], process, voltage, and temperature (PVT) variations [35], and circuit topologies [33], albeit with some trade-off in accuracy.

Alternatively, a topology-aware representation in [43] is proposed to reduce dataset size. With that approach, a GNN is combined with text embeddings of circuit components and a subcircuit-wise multi-head self-attention layer. The normalized Euclidean distance between every pair of devices in custom-designed FinFET analog layouts is computed in self-supervised manner. As a result, the learned latent-space distances mimic real spatial distances, with a wire-

length prediction accuracy of $R^2 \sim 57\%$ and net parasitic-capacitance prediction with sMAPE of 11.8%. Ultimately, the dataset size is reduced from 1,000 – 10,000 to about 450 simulated layout samples. Furthermore, lumped capacitance of voltage regulators, amplifiers, and serial link interconnects are modeled in [36], achieving an R^2 score of 77.2%. Coupling capacitance and parasitic resistance are incorporated in [38], improving the R^2 score by up to 87%. Chip-scale interconnect capacitance has been extracted in [37] with absolute average relative errors of $< 10\%$. The most representative ML-based techniques, along with their strengths and limitations, are summarized in Table I. Based on the qualitative comparison, [39] is the most promising approach for fast and accurate performance prediction in RFICs. A primary objective of the proposed framework is to simultaneously increase the prediction accuracy and reduce simulation overheads compared to [39].

Applying existing GNNs developed for analog circuits to RF systems presents several challenges, including nonlinearity and strong component dependencies (e.g., matched pairs, feedback loops) leading to high-tailed, skewed and multi-modal distributions of FoMs—characteristics that are difficult to model with simple NNs. To address the heavy-tailed distribution of parasitic capacitance values, a logarithmic normalization to stabilize variance and improve learning is applied in [42]. Even with this preprocessing, the GNN model trained to predict net-level parasitic capacitances of a VCO exhibits a relative error of 20%, underscoring the need for more accurate modeling techniques. An impressive $R^2 > 80\%$ in predicting key performance metrics across a variety of RF circuits, including LNAs, VCOs, mixers, and PAs is achieved in [39]—the top-performing GNN-based approach in RFIC EDA. However, this performance comes at the cost of training on $\sim 36,000$ samples of simulated circuits—a prohibitively high computational cost. It is worth noting that the large dataset size in [39] stems

from its circuit-to-graph embedding scheme—a significant limitation addressed in this paper by the embedding scheme, as described in Section III. Moreover, modeling nets and component pins as graph nodes and edges, respectively, complicates compatibility with other approaches (e.g., [40]) that represent components as nodes and nets as edges, enabling graph-based circuit identification via adjacency matrices. Embedding pins into edges also obscures critical pin-level details—such as source/drain/gate roles and layout symmetry—which are essential for effective circuit partitioning and parallelized simulation [41]. As a result, architectures that adopt this common pin/net embedding typically yield larger, more complex models and require significantly more training data to learn these distinctions implicitly. Alternatively, the proposed circuit embedding achieves comparable accuracy with significantly fewer training samples. Extensive synthetic data generation, as required in [39], is a bottleneck to the model scaling to real-world designs.

III. PROPOSED FRAMEWORK

The proposed end-to-end framework for predicting RF circuit performance metrics directly from netlist-derived graph representations is described in this section. First, the translation of RF circuits into annotated graphs is formalized to capture both inter-component relationships and global structure. Then, the GNN architecture designed to process these graphs is presented, enabling scalable, multi-hop aggregation of circuit context and flexible probabilistic modeling of diverse performance targets.

A. Graph Representation of RF Circuits

Each RF circuit is represented as an undirected graph where graph nodes correspond to component pins, and graph edges encode electrical connectivity. Pins of the same component (e.g., transistor source, drain, gate, and body bias terminals) are fully connected, forming a subgraph, easily

TABLE I: Comparison of State-of-the-Art ML Frameworks.

| Work | Key Architectural Features | Target Circuits | Average Training Size | Circuit Limitations | Other Limitations |
|------|------------------------------|----------------------------------|--------------------------------|---------------------|---|
| [39] | GNN | LNA, Mixer, VCO, PA, VA | $\sim 36k$ per circuit | — | Large synthetic data; Obscures sub-circuits; Struggles with multi-modality |
| [32] | GNN + TL | Resistor ladders, VA | 20k + 126k | simple analog | Overall, mediocre accuracy; Inaccurate for complex RF metrics |
| [43] | GNN + Text Embedding + Attn | VA | 1,177 | simple analog | Overall, mediocre accuracy; Inaccurate for complex RF metrics |
| [22] | CNN + LSTM | two-port RF filters | 8k per circuit | passive | Prohibitive data size; Lacks pin-level hierarchy support for unseen designs |
| [23] | Convolutional AE + Regressor | Band-pass filter | 5,929 + 916 | passive | Lacks pin-level hierarchy support for unseen designs |
| [17] | CNN + GA | PA matching networks | 500k + 170k | passive | Prohibitive data size; Lacks pin-level hierarchy support for unseen designs |
| [19] | DeepGRU + Dropout | VA, VCDL, DLL | ~ 9 waveforms per circuit | analog | Inaccurate for complex RF metrics; Lacks pin-level hierarchy support |
| [20] | DeepRNN | High-speed interconnects | 45 waveforms | passive | Lacks pin-level hierarchy support for unseen designs |
| [25] | Physics-aware S-TCNN | High-speed digital interconnects | $\sim 550-750$ per circuit | passive | Lacks pin-level hierarchy support for unseen designs |

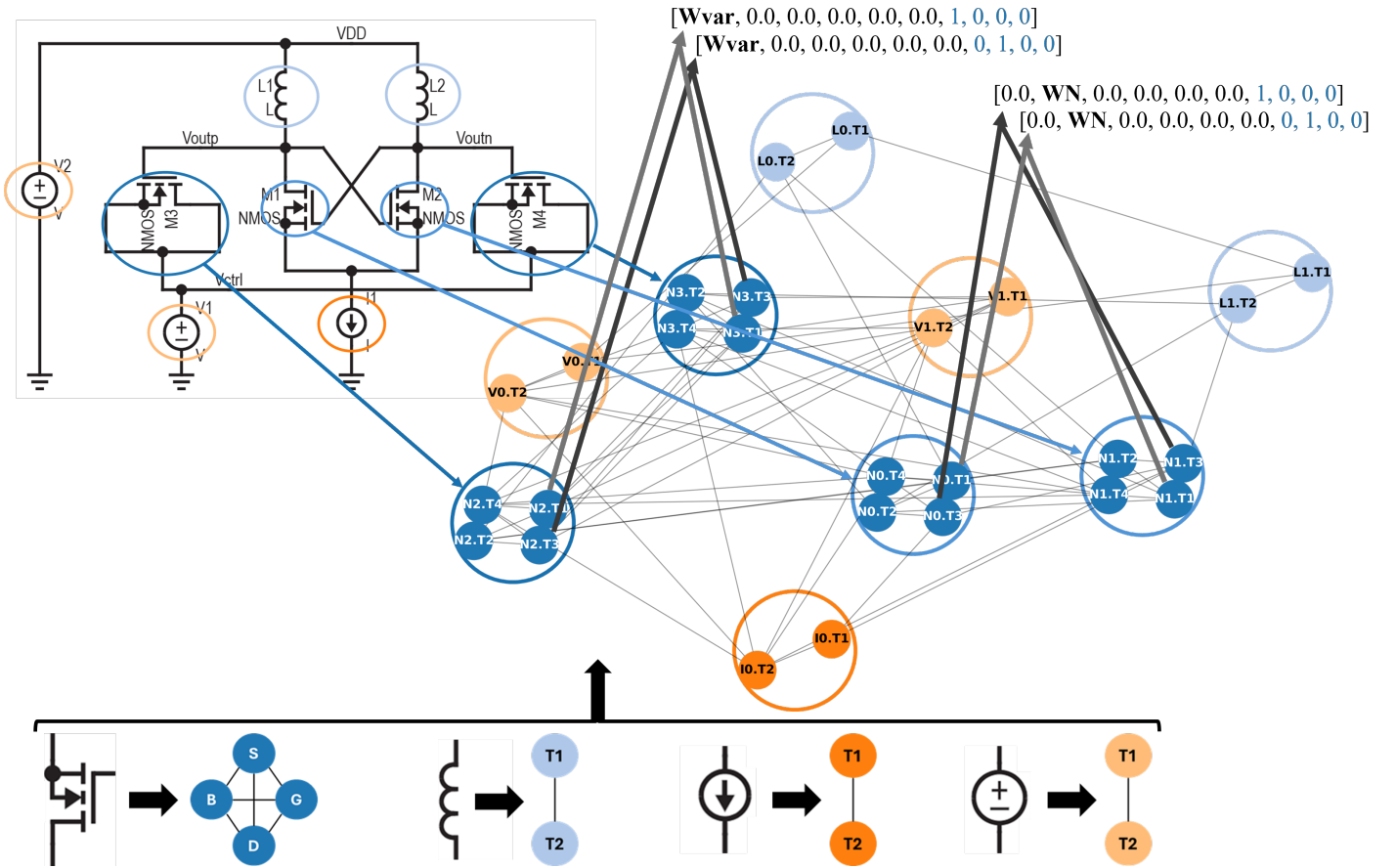


Fig. 1: Proposed circuit-to-graph conversion and feature extraction method, enabling symmetry preservation in RFICs.

distinguishable for future divide-and-conquer simulation attempts, as explained in Section II. Unlike a *pin-collapsed* representation where all terminals of a component are merged into a single node or edge, the proposed *pin-level* approach preserves terminal-level granularity. This allows each pin to be contextually linked to its functional counterparts, improving the encoding of signal flow and inter-component interactions. It also facilitates the incorporation of interconnect and layout parasitic information directly on graph edges.

Each graph node (i.e., component terminal) is annotated with a feature vector, encoding physical parameters such as transistor width×fingers and length, power supply levels, as well as resistor, capacitor, and inductor impedances. Each circuit component is assigned a unique index in the feature vector space, except for structurally and functionally symmetric components, which are intentionally mapped to the same index to preserve design equivalence and reduce redundancy. As depicted in Fig. 1, differential pair transistors (M1 and M2) serve a different purpose than NMOS varactors (M3 and M4), and this circuit symmetry is captured by positioning the individual devices’ features (e.g., width×fingers) in different feature vector indices. The same approach applies to all the components. For example, if the same design in Fig. 1 included choking inductors, a separate index would be assigned to capture their inductance features, distinct from the index used for the tank circuit inductors (L1 and L2 in the figure). This

tailored feature engineering imparts circuit design intuition to the model. One-hot encoding is employed to represent terminal’s position within a component (e.g., ‘1000’ for gate, ‘0100’ for source), allowing the model to distinguish current flow direction and identify the functional roles of terminals, such as source, gate, drain, and body. This distinction enhances prediction accuracy. A schematic illustration of the graph conversion is shown in Fig. 1.

B. GNN Architecture

The architecture of the proposed model is shown in Fig. 2. The netlist-derived graph is used as input to the GNN, which consists of four GENConv layers followed by a prediction head that outputs a circuit-specific performance metric. The GENConv hidden layers employ a softmax-weighted combination of candidate pooling behaviors, allowing the network to adaptively emphasize either distributed or dominant interactions, depending on the local circuit context. Intuitively, in a stack of four GENConv layers that enable effective local-to-global aggregation across the graph, the following behavior is observed:

- **First layer (1-hop neighborhood):** A terminal aggregates signals from other terminals of the same component and from directly connected nets. This supports pin-level property inference (e.g., drive strength, capacitive loading).

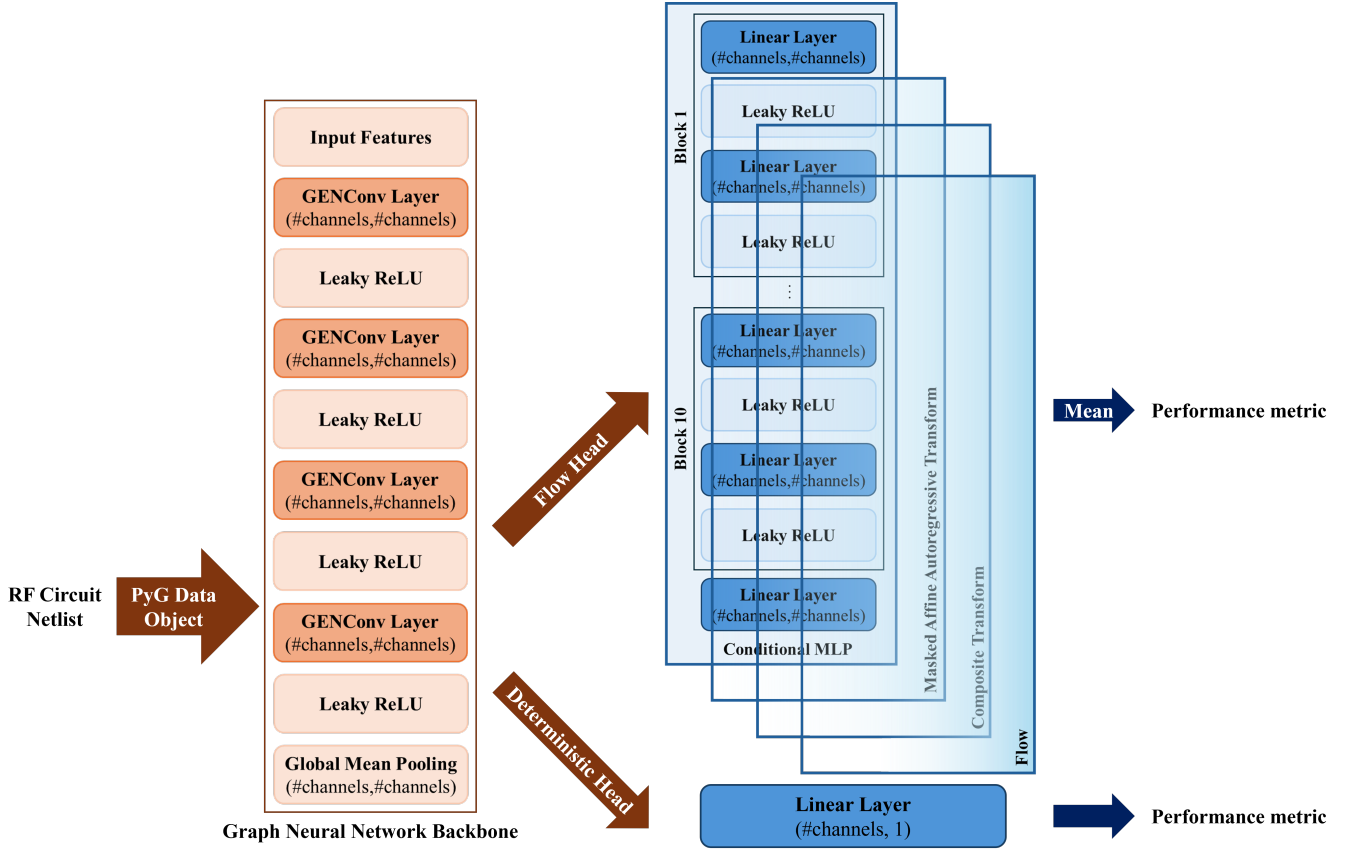


Fig. 2: Model architecture

- **Second layer (2-hop neighborhood):** Through an additional message-passing step, the terminal receives information from adjacent components, enabling the modeling of inter-component interactions such as matching networks and load-pull behavior.
- **Third layer (3-hop neighborhood):** At this stage, information propagates across short multi-stage paths, local feedback loops, or cascaded gain blocks. This captures subcircuit-level effects such as inter-stage loading, peaking networks, and first-order crosstalk.
- **Forth layer (4-hop neighborhood):** The receptive field expands to encompass components and nets involved in longer functional chains or distributed networks, providing context for block-level behavior such as biasing or matching networks, power-supply routing, and far-end impedance in RF microstrip lines. At this range, the model captures system-level couplings that affect timing closure, supply-induced noise, and stability margins.

Let $G = (V, E)$ be a graph where node v has features $h_v \in \mathbb{R}^d$ and $h_v^{(\ell, i)}$ is the hidden representation of node v at layer ℓ and iteration i . The message passed from node u to node v at layer ℓ and output i , a given circuit metric, is

$$m_{uv}^{(\ell, i)} = \phi_{\text{msg}}^{(\ell, i)}(h_u^{(\ell, i)}), \quad (1)$$

where ϕ_{msg} is a learnable function, trained via gradient descent. The message denotes an incremental stimulus propagated

from terminal represented by $u \in V$ to its adjacent terminal $v \in V$, modulated by the local characteristics of the device associated with u . Attention weights across neighbor nodes are computed using a softmax operation in GENConv layers where $a(\cdot, \cdot)$ is a learned scoring function that evaluates the compatibility between hidden features of the source node u and node v , yielding

$$\alpha_{uv}^{(\ell, i)} = \frac{\exp(a^{(\ell, i)}(h_u^{(\ell, i)}, h_v^{(\ell, i)}))}{\sum_{k \in \mathcal{N}(v)} \exp(a^{(\ell, i)}(h_k^{(\ell, i)}, h_v^{(\ell, i)}))}, \quad (2)$$

where $\mathcal{N}(v)$ is the set of neighboring nodes of v . Intuitively, the attention weight $\alpha_{uv}^{(\ell, i)}$ plays the role of a normalized admittance $g_{uv} / \sum g_{uv}$, whereby neighbors with higher conductance (and thus, higher current) exert greater influence on the nodal aggregation. The aggregated message is, therefore,

$$M_v^{(\ell, i)} = \sum_{u \in \mathcal{N}(v)} \alpha_{uv}^{(\ell, i)} m_{uv}^{(\ell, i)}, \quad (3)$$

To help clarify how GNNs mimic physical principles (e.g., superposition and local conservation laws) when modeling circuit behavior, consider the following analogy to the net current mismatch encountered during Newton-Raphson iterations in circuit simulation. In these solvers, Kirchhoff's current law (KCL) is enforced by iteratively adjusting node voltages

to minimize the total current imbalance at each node. The net mismatch refers to the residual current that remains after evaluating all branch currents based on the current voltage estimate—an indicator of how far the solution is from satisfying KCL. In the context of message passing in GNNs, coefficients such as $\alpha(\cdot, \cdot)$ regulate how strongly one node influences another, similar to how conductance determines current flow in a circuit. The imbalance in aggregated messages at a node, before being resolved by the model’s update function, resembles the net current mismatch before a Newton update. Thus, just as the Newton update uses the mismatch to refine voltage guesses, the learnable functions in the GNN refine node embeddings to better encode local electrical behavior and global circuit context.

Each layer l applies a nonlinear transformation to its inputs at iteration i , producing the hidden representation for iteration $(i + 1)$, without residual connections,

$$h_v^{(\ell+1,i)} = \text{LeakyReLU}_{0.1}(M_v^{(\ell,i)}), \quad (4)$$

$$\ell = 0, \dots, L-1, \quad i = 1, \dots, H.$$

The LeakyReLU activation with the slope of 0.1 serves as an analogy to a piecewise-linear I–V characteristic: its positive-slope region mimics the forward-conducting path of a device, while the small negative-slope “leak” term prevents node isolation—functionally resembling a large shunt resistance that electrically anchored otherwise floating nodes.

Stacking L such layers is therefore analogous to cascading L successive linearization-and-update steps, similar to those performed in a nonlinear AC small-signal solver. These layers update the node-level embeddings, which are then aggregated to form a single graph-level embedding,

$$h_G^{(i)} = \text{MeanPool}\{h_v^{(L,i)} : v \in V\} = \frac{1}{|V|} \sum_{v \in V} h_v^{(L,i)}, \quad (5)$$

where MeanPool is the global mean pooling operation. Such pooling aggregates all terminal-level embeddings to produce a reduced-order macro-model, representing the entire circuit’s metric with a single vector $h_G^{(i)}$. Finally, each output head f_i maps $h_G^{(i)}$ to a prediction for the i -th circuit metric,

$$\hat{y}^{(i)} = f_i(h_G^{(i)}). \quad (6)$$

For deterministic outputs (e.g., DC power), f_i is linear,

$$\hat{y}^{(i)} = \mathbf{w}^{(i)\top} h_G^{(i)} + b^{(i)}. \quad (7)$$

A linear projection resembles Ohm’s law or other first-order physical relationships where the output metric scales proportionally with the aggregated input variables.

For probabilistic outputs (e.g., phase noise), a conditional normalizing flow model, Flow $_{\theta}$ [47] is used to predict the output distribution for f_i ,

$$p_{\theta}^{(i)}(y_i | h_G^{(i)}) = \text{Flow}_{\theta}^{(i)}(y_i; h_G^{(i)}). \quad (8)$$

By conditioning the flow on the circuit’s embedding, the model learns to adapt its predicted distribution to each individual design, providing a flexible and expressive surrogate for uncertainty-aware performance estimation. Unlike simple regression models that assume Gaussian outputs, normalizing flows can model complex statistical properties, including multi-modal distributions with unknown number of heads as well as non-Gaussian skewed or heavy-tailed distributions that are often observed in RF circuits.

Based on the empirical distribution of each performance metric, the model assigns either a deterministic or probabilistic output head. For near-linear metrics such as DC power consumption, a deterministic output head is employed to produce a scalar prediction \hat{y}_i via a linear projection without explicitly modeling uncertainty.

On the other hand, for metrics exhibiting significant non-linearity or statistical variation (e.g., phase noise and tuning range), a conditional flow head generates a full predictive distribution, enabling uncertainty-aware estimation tailored to each individual design. The flow head implemented as a single MAF layer [48] consisting of ten autoregressive blocks. Each block is an MLP conditioned on the pooled graph embedding h_i , enabling the modeling of complex, skewed, and multi-modal conditional distributions. MAF offers a principled approach to flexible density estimation, combining tractable likelihoods, efficient (linear-time) gradient computation, and universal function approximation. This allows the model to learn probabilistic non-Gaussian behaviors often observed in RFICs. Due to its novel application in circuit modeling, this output head is discussed in further detail below.

C. Masked Autoregressive Flow

MAF belongs to the normalizing flows class [49], which model complex probability distributions by transforming a simple base distribution (e.g., a standard Gaussian) through a sequence of invertible and differentiable functions. The masked autoregressive structure of MAF ensures that each variable depends only on preceding variables in a specified ordering. This dependency is enforced using masking, which leads to a triangular Jacobian matrix of the transformation. The triangular form is critical because it allows the log-determinant of the Jacobian (needed for exact likelihood evaluation in flow-based models) to be computed efficiently as the sum of the diagonal terms. In this section, the key definitions are reviewed, intuitive insights into the approach are provided, and the suitability of MAF for modeling diverse and complex performance distributions in RFICs is discussed.

Let $y \in \mathbb{R}^D$ be the target variable and $h \in \mathbb{R}^M$ a conditioning context in D and M dimensional spaces, respectively. Given the complex conditional density $p_{\theta}(y | h)$, MAF transforms y into a simpler latent space with known distribution (e.g., Gaussian. $p_Z(z) = \mathcal{N}(0, I)$) using a learned invertible, autoregressive mapping $f_{\theta}(\cdot; h) : \mathbb{R}^D \rightarrow \mathbb{R}^D$. The conditional density is therefore expressed as,

$$p_{\theta}(y | h) = p_Z(f_{\theta}(y; h)) |\det \nabla_y f_{\theta}(y; h)|. \quad (9)$$

In contrast to classical parametric families that impose linear covariance structures, MAF learns nonlinear coordinate transformations that locally stretch or compress space. This enables the modeling of skewed, heavy-tailed, or multimodal conditional densities. The determinant in Eq. (9) adjusts the probability mass accordingly, while preserving tractable and exact likelihood evaluation. MAF, therefore, transforms y as,

$$z_i = \frac{y_i - \mu_{\theta,i}(y_{<i}; h)}{\sigma_{\theta,i}(y_{<i}; h)}, \quad i = 1, \dots, D, \quad (10)$$

where the mean $\mu_{\theta,i}$ and standard deviation $\sigma_{\theta,i} > 0$ are outputs of masked, autoregressive MLPs conditioned on $y_{<i}$ and h . Since analytic integration is intractable, the conditional mean $\mathbb{E}[Y \mid h]$ is estimated via Monte-Carlo sampling, yielding low-variance estimates with relatively few samples,

$$\hat{\mathbb{E}}[Y \mid h] = \frac{1}{S} \sum_{s=1}^S y^{(s)}, \quad y^{(s)} \sim p_{\theta}(\cdot \mid h). \quad (11)$$

Since each z_i depends only on $y_{<i}$, the Jacobian, $\nabla_y f_{\theta}$, is triangular, leading to a tractable log-determinant,

$$\log \left| \det \nabla_y f_{\theta}(y; h) \right| = - \sum_{i=1}^D \log \sigma_{\theta,i}(y_{<i}; h). \quad (12)$$

Given a dataset $\{(y_i, h_i)\}_{i=1}^N$, the parameters are learned by maximizing the conditional log-likelihood:

$$\mathcal{L}_{\text{flow}}(\theta) = - \frac{1}{N} \sum_{i=1}^N \log p_{\theta}(y_i \mid h_i). \quad (13)$$

To improve expressiveness, K flow layers are stacked with intermediate variable permutations, resulting in a composite transformation d_{θ} that serves as a universal approximator of continuous probability densities,

$$g_{\theta}(y) = f_{\theta}^{(K)} \circ \dots \circ f_{\theta}^{(2)} \circ f_{\theta}^{(1)}(y). \quad (14)$$

Each layer incrementally warps the latent space to introduce complex dependencies, while permutations ensure that all variables can condition on each other across the stack, overcoming the fixed autoregressive ordering of individual layers.

IV. EXPERIMENTAL SETUP

Experimental setup is outlined in this section, including the training strategy, loss formulations, data preprocessing and augmentation, and computational settings. These framework components are designed to enable robust training, effective regularization, and reproducible results.

A. Framework Architecture

MAF is conditioned on pooled graph embeddings produced by four stacked GENConv layers, with the individual LeakyReLU activations and a global mean pooling. For outputs requiring flexible uncertainty-aware estimation, a MAF head layer is designed with context features as extracted from the graph encoder. Each transformation employs two hidden

blocks with LeakyReLU activations and 128 hidden features per layer. Flows are initialized near the identity transformation by setting $\mu = 0$, $\log \sigma = 0$, which facilitates stable optimization during the early training stages. The computational complexity of the proposed framework is $\mathcal{O}(KD)$ per sample during training or inference, where K is the number of flow layers and D is the output dimensionality. For probabilistic targets, sampling is performed independently across batch elements and Monte Carlo samples drawn from the predicted distribution. As mentioned earlier, deterministic scalar heads are used for unimodal targets.

B. Training and Lightweight Computations

All experiments are performed on a single NVIDIA GeForce RTX 4090 GPU using floating-point 32 precision. This setup maintains hardware agnosticism, facilitates debugging, and provides sufficient computational speed for the network size considered. Reproducibility is ensured by fixing random seeds across all relevant libraries and disabling residual nondeterminism in CUDA Deep Neural Network (cuDNN) kernels.

Training is performed end-to-end using the weighted Adam (AdamW) optimizer. The learning rate is reduced by a factor of two with the ReduceLRonPlateau scheduler if the median validation loss does not improve for five consecutive epochs. Early stopping is applied individually to each output head: a given prediction head is frozen if it shows no improvement for ten consecutive epochs, while training continues for the remaining heads. This strategy accommodates varying convergence rates across different performance metrics, preserving model capacity for more challenging targets while avoiding overfitting on simpler ones.

Deterministic outputs are trained by minimizing mean squared error (MSE) and evaluated using the coefficient of determination (R^2) on the original scale—that is after applying the inverse transformation of the z-score standardization. Probabilistic outputs are modeled with conditional normalizing flows, trained by minimizing negative log-likelihood. For probabilistic outputs, mean relative error (MRE) is also computed on the original inverse-transform scale for both validation and inference. Additionally, relative error percentiles and thresholds-based accuracy metrics are reported for all outputs.

Netlists and constant parameters (e.g., power supply voltage V_{DD} and reference current I_{ref}) are parsed only once at start-up and cached as Python dictionaries (i.e., hash-maps). Subsequent device-level sizing values and simulation results, stored in a .CSV file, are normalized once. ProcessPoolExecutor is launched to map .CSV rows to parallel threads (aka workers). Template objects, such as node names and edge indices, are initialized once in the main process and shared with worker processes to avoid repeated setup overhead. The resulting graphs are then saved to disk for efficient data transfer. Node features are min-max-scaled while targets are z-standardized. Statistics are computed on the training split only and reused for validation and test, eliminating leakage of unseen data. During training, a $\mathcal{N}(0, 0.01)$ noise is added to discourage memorizing and overfitting, increasing the frame-

TABLE II: Performance on Power Amplifiers (PAs). Average Training Size: 21,087 Simulated Samples.

| Benchmark | P_{DC} | S_{11} | S_{22} | P_{Gain} | DE | PAE | P_{SAT} |
|-----------|----------|----------|----------|------------|--------|--------|-----------|
| R^2 | 99.94% | N/A | N/A | N/A | N/A | N/A | 99.72% |
| MRE | 0.31% | 4.32% | 4.40% | 2.11% | 1.74% | 3.15% | 7.43% |
| MRE P75 | 0.45% | 5.93% | 5.71% | 2.02% | 2.33% | 2.62% | 3.67% |
| MRE P90 | 0.55% | 8.21% | 9.40% | 3.95% | 3.97% | 4.91% | 9.01% |
| MRE <2% | 100.00% | 48.37% | 46.14% | 81.50% | 76.79% | 69.83% | 67.97% |
| MRE <5% | 100.00% | 75.17% | 75.19% | 93.26% | 90.92% | 90.32% | 84.33% |
| MRE <20% | 0.00% | 2.93% | 3.07% | 1.20% | 0.39% | 1.08% | 3.68% |
| NRMSE | 0.40% | N/A | N/A | N/A | N/A | N/A | 2.62% |
| sMAPE | 0.31% | 4.23% | 4.34% | 1.97% | 1.74% | 2.37% | 4.51% |

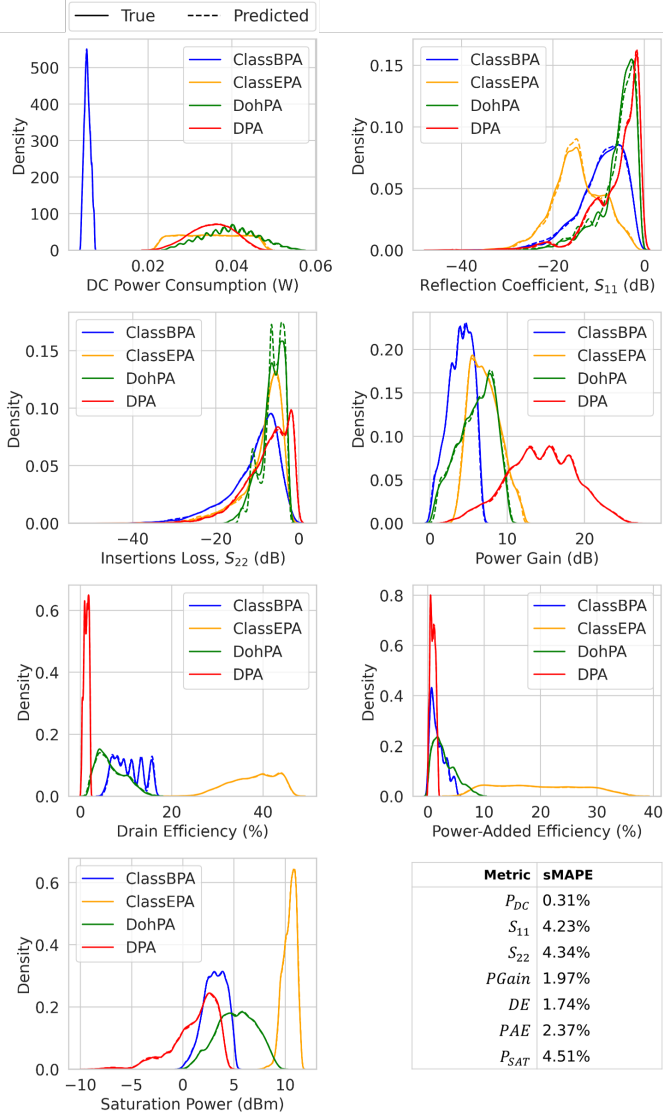


Fig. 3: KDE plots of true and predicted values of power amplifiers (PAs).

work accuracy. The noise also facilitates smoother gradients, improves second-moment estimates in AdamW, and enables gradient-based interpretability.

The framework exploits two PyTorch libraries: graph layers are employed from PyTorch Geometric [50] and MAF from the nflows library [51]. All components are compatible with CUDA 12.5 or later, requiring no additional setup.

TABLE III: Relative Performance on Mixers. Average Training Size: 13,481 Simulated Samples.

| Benchmark | P_{DC} | C_{Gain} | NF | V_{swg} |
|-----------|----------|------------|---------|-----------|
| R^2 | 99.90% | 99.03% | 99.90% | 99.86% |
| Avg. MRE | 0.63% | 6.55% | 0.23% | 1.21% |
| MRE P75 | 0.90% | 1.97% | 0.32% | 1.54% |
| MRE P90 | 1.20% | 4.15% | 0.47% | 2.22% |
| MRE <2% | 96.42% | 77.38% | 99.98% | 80.84% |
| MRE <5% | 100.00% | 91.35% | 100.00% | 96.53% |
| MRE >20% | 0.00% | 1.95% | 0.00% | 0.01% |
| NRMSE | 0.65% | 2.92% | 0.28% | 1.55% |
| sMAPE | 0.62% | 2.55% | 0.23% | 1.21% |

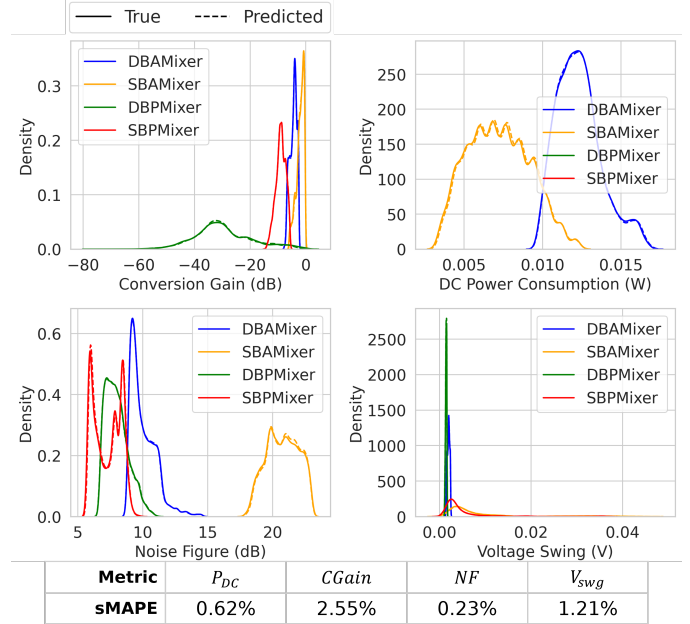


Fig. 4: KDE plots of true and predicted values of mixers.

C. Dataset Description

A publicly available dataset first introduced in [39] is used. The dataset comprises over one million Cadence-simulated analog and RF circuits of various topologies such as single- and double-balanced active (SBAMixer, DBAMixer) and passive (SBPMixer, DBPMixer) mixers; cross-coupled (CCVCO), Colpitts (CoLVCO), inductive-feedback (IFVCO), and ring (RVCO) VCOs; common-source (CSLNA), common-gate (CGLNA), and differential (DLNA) LNAs; as well as class-B (ClassBPA), class-E (ClassEPA), differential (DPA), and Doherty (DohPA) PAs. The training/validation/test ratio of 50%/25%/25% is chosen for the CSA, 80%/10%/10% for the CVA, and 30%/35%/35% for all other circuits.

Each data point includes netlists, parameter sweeps, and simulation results spanning key performance metrics such as power gain (P_{Gain}), conversion gain (C_{Gain}), bandwidth (BW), noise figure (NF), DC Power Consumption (P_{dc}), drain efficiency (DE), saturation power (P_{SAT}), oscillation frequency (f_{osc}), tuning range (TR), output power (P_{out}), phase noise (PN), voltage swing (V_{swg}), power-added efficiency (PAE), and S-parameters at the fundamental frequency.

TABLE IV: Performance on Voltage-Controlled Oscillators (VCOs). Average Training Size: 17,482 Simulated Samples.

| Benchmark | P_{DC} | f_{osc} | TR | P_{out} | PN |
|-----------|----------|-----------|--------|-----------|--------|
| R^2 | 99.96% | 93.81% | N/A | N/A | N/A |
| Avg. MRE | 0.22% | 0.98% | 7.86% | 7.43% | 1.44% |
| MRE P75 | 0.30% | 1.20% | 9.12% | 3.99% | 1.74% |
| MRE P90 | 0.39% | 2.37% | 15.13% | 8.62% | 3.28% |
| MRE <2% | 100.00% | 88.15% | 50.15% | 68.66% | 82.20% |
| MRE <5% | 100.00% | 96.82% | 74.80% | 80.00% | 93.23% |
| MRE >20% | 0.00% | 0.13% | 9.27% | 4.09% | 0.40% |
| NRMSE | 0.27% | 1.86% | N/A | N/A | N/A |
| sMAPE | 0.22% | 0.98% | 6.83% | 4.31% | 1.42% |

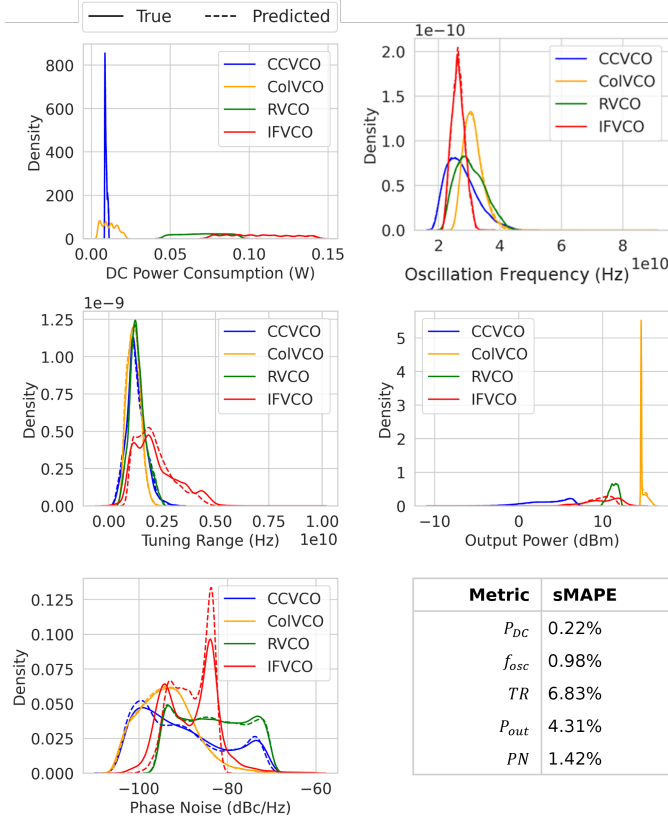


Fig. 5: KDE plots of true and predicted values of voltage-controlled oscillators (VCOs).

V. RESULTS AND DISCUSSION

The proposed GNN framework is evaluated on multiple topologies across four primary RFIC classes: LNAs, mixers, VCOs, and PAs. The overall framework accuracy is evaluated using standard relative benchmarks such as (i) R^2 score, (ii) mean relative error (MRE) reported within 2% and 5% error thresholds and for 75th and 90th percentiles (P75 and P90), (iii) normalized root mean square error (NRMSE), and (iv) symmetric mean absolute percentage error (sMAPE). The accuracy benchmarks are determined based on the non-scaled (i.e., inverse-transformed as needed), actual target values. For unimodal RFIC performance metrics, characterized by a well-defined mean, mean-based evaluation benchmarks such as R^2 and NRMSE are reported. For multimodal or skewed RFIC metrics, such simpler benchmarks can however be misleading. In these cases, model accuracy is reported using

TABLE V: Relative Performance on Low Noise Amplifiers (LNAs). Average Training Size: 18,269 Simulated Samples.

| Benchmark | BW | P_{DC} | S_{11} | NF | P_{Gain} |
|-----------|--------|----------|----------|---------|------------|
| R^2 | N/A | 99.96% | N/A | N/A | N/A |
| Avg. MRE | 0.85% | 0.84% | 4.22% | 0.44% | 8.96% |
| MRE P75 | 1.14% | 0.81% | 5.75% | 0.62% | 4.91% |
| MRE P90 | 1.80% | 2.33% | 9.77% | 0.92% | 14.49% |
| MRE <2% | 92.30% | 93.25% | 42.21% | 98.58% | 49.03% |
| MRE <5% | 99.62% | 96.52% | 75.51% | 100.00% | 74.76% |
| MRE >20% | 0.00% | 0.00% | 2.67% | 0.00% | 5.87% |
| NRMSE | N/A | 0.58% | N/A | N/A | N/A |
| sMAPE | 0.98% | 0.87% | 4.23% | 0.44% | 7.63% |

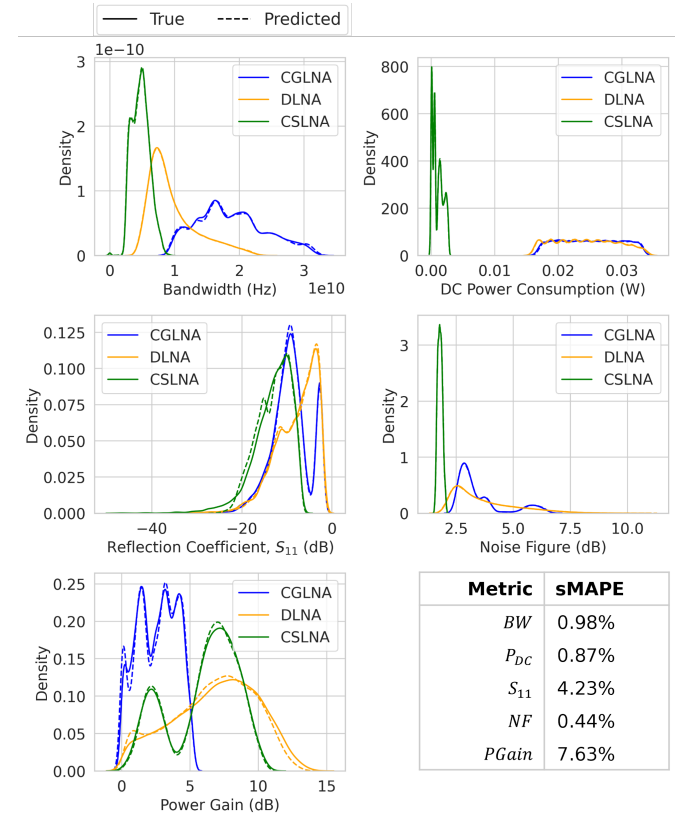


Fig. 6: KDE plots of true and predicted values of low noise amplifiers (LNAs).

MRE, percentiles, and sMAPE benchmarks. MRE penalizes large predicted values corresponding to small true values more heavily than it penalizes small predicted values corresponding to large true values. Consequently, for performance metrics such as V_{Gain} or P_{out} , which often include near-zero dB values, MRE can be unstable and unreliable.

For intuition, consider the C_{Gain} metric of mixers: the simulated and predicted waveforms in Fig. 4 indicate good agreement, and the metric is well-predicted with a sMAPE of 2.55% and 90% of MRE values below 4.15% (see Table III). However, the average MRE is disproportionately inflated to 6.55% due to divisions-by-zero. In contrast, sMAPE incorporates both the true and predicted values symmetrically in the denominator, treating them equivalently. Thus, to provide a more consistent and interpretable comparison across diverse targets, sMAPE is adopted as the unified evaluation metric.

TABLE VI: Performance on Voltage Amplifiers (VAs). Average Training Size: 11,705 Simulated Samples.

| Benchmark | BW | P _{DC} | V _{Gain} |
|-----------|--------|-----------------|-------------------|
| R^2 | N/A | 99.38% | N/A |
| Avg. MRE | 3.44% | 4.09% | 6.40% |
| MRE P75 | 3.78% | 4.85% | 2.48% |
| MRE P90 | 7.61% | 9.42% | 8.20% |
| MRE < 2% | 52.90% | 47.17% | 72.09% |
| MRE < 5% | 79.67% | 77.27% | 88.42% |
| MRE > 20% | 2.19% | 2.97% | 3.39% |
| NRMSE | N/A | 4.15% | N/A |
| sMAPE | 3.57% | 6.41% | 3.83% |

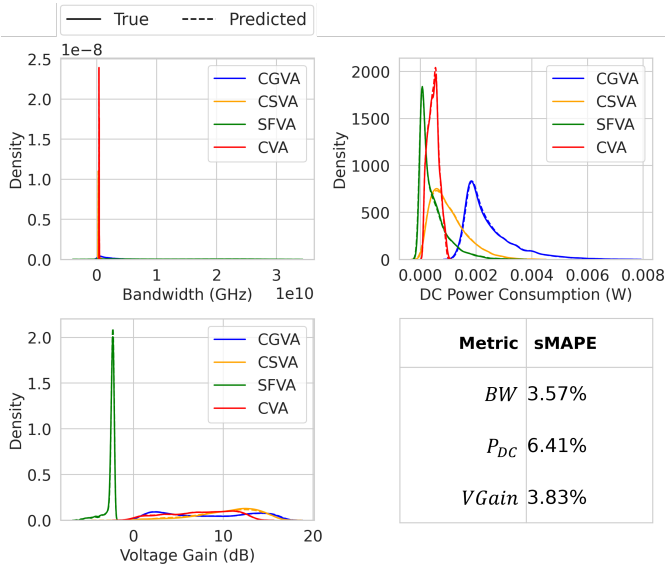


Fig. 7: KDE plots of true and predicted values of voltage amplifiers (VAs).

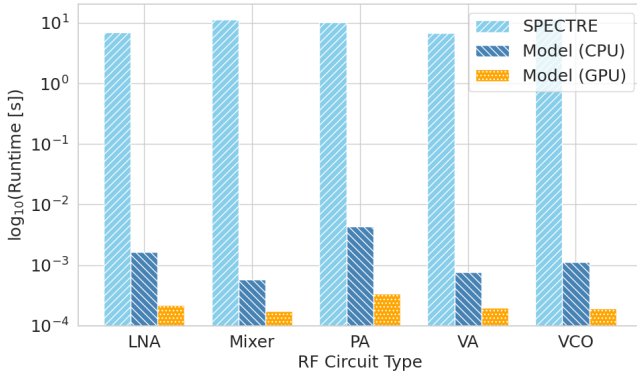


Fig. 8: Comparison of inference time needed on different RF circuits (LNA, Mixer, PA, VA, and VCO) on Spectre (6.73-11.69 seconds) versus the model on CPU (0.57-4.37 seconds) and GPU (0.17-0.34 milliseconds).

The empirical densities of both the ground truth and model predictions are shown using kernel density estimate (KDE) plots¹ in Figs. 3–7 visualize the empirical density of both the true values gathered through SPICE-simulations and the

¹A KDE is a non-parametric estimate of a probability density function obtained by centering smooth kernel functions (e.g., Gaussian) on every sample and summing their contributions.

predicted values by the model. A close match between the two curves indicates that the proposed surrogate accurately captures the conditional distributions of the underlying metrics. This strong alignment attests to the effectiveness of the training setup and confirms that the model produces well-calibrated, distribution-aware predictions for both unimodal and multimodal RF FoMs.

Corresponding numerical results are listed in Tables II–VI, exhibiting an MRE of less than $\sim 2.63\%$ and sMAPE of less than $\sim 2.17\%$ for majority of circuits and RF metrics. This validates the model’s ability to capture nonlinear, skewed, and multimodal target distributions. Cascode LNA (CLNA) with relatively lower feature importance values, is the only circuit out of 20 to show poor results. As shown in Fig. 9, richer features other than sizing values (e.g., intermediate SPICE simulation results or relevant performance metrics) should be added for CLNA. Identified as an outlier, CLNA results are not included in tables and remains subject to future work. Note that prior works are typically evaluated on fewer and simpler circuit topologies, with [39] reporting only average benchmark results rather than per-circuit performance metrics. In comparison, the average MRE reported in [39] is 9.14%, while the proposed framework achieves 2.91% (without the CLNA) and 5.83% (with the CLNA) with $2.22\times$ reduction in data. sMAPE of all circuits (with the CLNA) is 4.06%.

Compared to an average 9.384 s simulation runtime with Spectre, the proposed model reduces on average the per-circuit runtime from to 1.687 ms if ran on CPU and 0.225 ms if ran on GPU. This is a speedup of $\sim 5,563\times$ with CPU and $\sim 41,707\times$ with GPU, as depicted in Fig. 8.

A. Comparison with State-of-the-Art

A comparison between the proposed method and existing ML-based circuit models is presented in Table VII. Relative to the best-performing prior work [39], the proposed framework reduces training data requirements by $\sim 2.24\times$, lowers average MRE from 9.14% to 2.91%, indicating superior data efficiency and predictive accuracy, and shows a competitive sMAPE of 2.40%. The proposed pin-level, symmetry-aware graph construction method supports subcircuit identification for scalable simulation. Relative to non-GNN methods, this approach uniquely generalizes to active RFICs while maintaining lightweight training costs.

B. Discussion of Limitations

Despite improved accuracy and data efficiency, the proposed approach has several limitations. First, while the pin-level graph representation reduces training data requirements, prediction accuracy can degrade for circuits with rare topologies, extreme parameters values not represented in the training set, or non-informative features. Second, the framework in its current version does not explicitly model layout parasitics which limits its applicability to post-layout performance estimation. Finally, integration with closed-loop design optimization and the use of active learning to further reduce training dataset size are left for future work.

TABLE VII: Performance Comparison of the Proposed Framework and FALCON [39]—The Most Promising SOTA Framework for RFIC Performance Prediction (see Table I).

| Metric | Work Unit | P _{DC} mW | V _{Gain} dB | P _{Gain} dB | C _{Gain} dB | S ₁₁ dB | S ₂₂ dB | NF dB | BW GHz | f _{osc} GHz | TR GHz | P _{out} dBm | PSAT dBm | DE % | PAE % | PN dBc/Hz | V _{swg} mV |
|--------|------------------|--------------------|----------------------|----------------------|----------------------|--------------------|--------------------|-------------|-------------|----------------------|-------------|----------------------|-------------|-------------|-------------|-------------|---------------------|
| MRE | This work | 1.3% | 6.4% | 5.0% | 6.5% | 4.3% | 4.4% | 0.3% | 2.3% | 1.0% | 7.9% | 7.4% | 7.4% | 1.8% | 3.5% | 1.4% | 1.2% |
| | FALCON | 11.5% | 2.7% | 18.6% | 7.8% | 11.4% | 1.8% | 4.5% | 5.6% | 0.6% | 6.5% | 4.4% | 4.5% | 4.5% | 11.7% | 1.3% | 1.5% |
| RMSE | This work | 0.10 | 0.32 | 0.15 | 0.53 | 0.81 | 0.69 | 0.03 | 0.14 | 0.55 | 0.19 | 0.60 | 0.08 | 0.18 | 0.09 | 2.21 | 0.10 |
| | FALCON | 0.29 | 0.11 | 0.54 | 0.84 | 1.52 | 0.21 | 0.53 | 0.97 | 0.72 | 0.29 | 0.91 | 0.10 | 0.23 | 0.14 | 2.54 | 0.07 |
| MAE | This work | 0.08 | 0.18 | 0.12 | 0.19 | 0.44 | 0.37 | 0.02 | 0.09 | 0.30 | 0.13 | 0.30 | 0.06 | 0.13 | 0.06 | 1.25 | 0.07 |
| | FALCON | 0.21 | 0.08 | 0.21 | 0.19 | 0.55 | 0.12 | 0.20 | 0.37 | 0.18 | 0.10 | 0.23 | 0.07 | 0.17 | 0.10 | 1.17 | 0.05 |

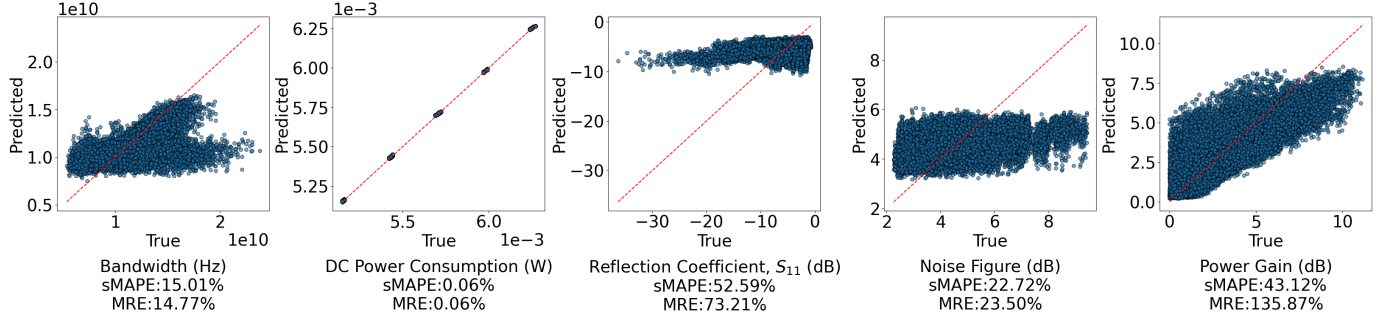


Fig. 9: True versus predicted values of the worst performing circuit, CLNA. Training Size: 18,669 Simulated Samples.

VI. CONCLUSION AND FUTURE WORK

A topology-aware pin-level GNN framework is presented for lightweight prediction of RFIC performance metrics LNAs, mixers, VCOs, and PAs. By representing circuit netlists at the pin-level, the proposed method preserves symmetry and functional distinctions, reducing data requirements and improving generalization compared to prior pin-collapsed approaches. Accurate modeling of multi-modal, skewed distributions often found in RF FoMs is enabled with masked autoregressive flows. Empirical results demonstrate strong predictive accuracy with an average sMAPE and MRE of, respectively, 2.40% and 2.91%, while using $2.24\times$ fewer training samples than prior art and running on average $41,707\times$ faster than Spectre simulation. Future work includes:

- Incorporating layout features to enable accurate post-layout parasitic modeling, including interconnect effects.
- Extending the model to predict frequency-continuous responses, such as full S-parameters plots.
- Embedding this model into automated RF design flow.
- Learning latent RFIC representations to support topology identification, optimization, and parallelizable simulation.

REFERENCES

- [1] O. Khan, A. Niknejad, and K. Pister, "Ultra low-power transceiver SoC designs for IoT, NB-IoT applications," in *Proceedings of the IEEE Custom Integrated Circuits Conference (CICC)*, 2018, pp. 1–77.
- [2] W. Hong, Z. H. Jiang, C. Yu, D. Hou, H. Wang, C. Guo, Y. Hu, L. Kuai, Y. Yu, Z. Jiang, Z. Chen, J. Chen, Z. Yu, J. Zhai, N. Zhang, L. Tian, F. Wu, G. Yang, Z.-C. Hao, and J. Y. Zhou, "The role of millimeter-wave technologies in 5G/6G wireless communications," *IEEE Journal of Microwaves*, vol. 1, no. 1, pp. 101–122, 2021.
- [3] S. H. Dokhanchi, B. S. Mysore, K. V. Mishra, and B. Ottersten, "A mmWave automotive joint radar-communications system," *IEEE Transactions on Aerospace and Electronic Systems*, vol. 55, no. 3, pp. 1241–1260, 2019.
- [4] H. Zheng, R. Ma, M. Liu, and Z. Zhu, "A linear-array receiver analog front-end circuit for rotating scanner lidar application," *IEEE Sensors Journal*, vol. 19, no. 13, pp. 5053–5061, 2019.
- [5] M. M. Gourary, S. G. Rusakov, S. L. Ulyanov, M. M. Zharov, and B. J. Mulvaney, "Circuit distortion analysis based on the simplified newton's method," *Journal of Electrical and Computer Engineering*, vol. 2011, no. 1, p. 540305, 2011.
- [6] X. Yang, Y.-S. Huang, L. Zhou, Z. Zhao, D.-X. Ni, C.-R. Zhang, J.-F. Mao, J.-A. Han, X. Cheng, and X.-J. Deng, "Low-loss heterogeneous integrations with high output power radar applications at W-band," *IEEE Journal of Solid-State Circuits (JSSC)*, vol. 57, no. 6, pp. 1563–1577, 2022.
- [7] J. Lee, W. Jia, B. S. Rodriguez, and J. S. Walling, "Pixelated RF: Random metasurface based electromagnetic filters," in *IEEE Interregional NEWCAS Conference (NEWCAS)*, 2023, pp. 1–5.
- [8] P. Vancorenland, C. De Ranter, M. Steyaert, and G. Gielen, "Optimal RF design using smart evolutionary algorithms," in *Proceedings of the IEEE/ACM Design Automation Conference (DAC)*, 2000, p. 7–10.
- [9] T. Pessoa, N. Lourenço, R. Martins, R. Póvoa, and N. Horta, "Enhanced analog and RF IC sizing methodology using PCA and NSGA-II optimization kernel," in *Proceedings of the Design, Automation & Test in Europe Conference & Exhibition (DATE)*, 2018, pp. 660–665.
- [10] Y. Hong, J. Huang, and J. Cai, "Design of broadband RF PAs using an improved bayesian optimization algorithm," *IEEE Transactions on Microwave Theory and Techniques*, pp. 1–13, 2025.
- [11] J. E. Rayas-Sanchez, S. Koziel, and J. W. Bandler, "Advanced RF and microwave design optimization: A journey and a vision of future trends," *IEEE Journal of Microwaves*, vol. 1, no. 1, pp. 481–493, 2021.
- [12] M. Larbi, R. Trincherro, F. G. Canavero, P. Besnier, and M. Swaminathan, "Analysis of parameter variability in an integrated wireless power transfer system via partial least-squares regression," *IEEE Transactions on Components, Packaging and Manufacturing Technology*, vol. 10, no. 11, pp. 1795–1802, 2020.
- [13] A. Mehradfar, X. Zhao, Y. Niu, S. Babakniya, M. Alesheikh, H. Aghasi, and S. Avestimehr, "Supervised learning for analog and RF circuit design: Benchmarks and comparative insights," 2025.
- [14] H. Chae, S. H. Chai, T. Chi, S. Li, and D. Z. Pan, "ML-assisted RF IC design enablement: the new frontier of AI for EDA," in *Proceedings of the Asia and South Pacific Design Automation Conference (ASP-DAC)*, 2025, p. 683–689.
- [15] K. Scharff, C. M. Schierholz, C. Yang, and C. Schuster, "ANN performance for the prediction of high-speed digital interconnects over

- multiple PCBs,” in *IEEE Conference on Electrical Performance of Electronic Packaging and Systems (EPEPS)*, 2020, pp. 1–3.
- [16] A. Sánchez-Masís, R. Rimolo-Donadio, K. Roy, M. Sulaiman, and C. Schuster, “FNNs models for regression of S-parameters in multilayer interconnects with different electrical lengths,” in *2023 IEEE MTT-S Latin America Microwave Conference (LAMC)*, 2023, pp. 82–85.
- [17] E. A. Karahan, Z. Liu, and K. Sengupta, “Deep-learning-based inverse-designed millimeter-wave passives and power amplifiers,” *IEEE Journal of Solid-State Circuits (JSSC)*, vol. 58, no. 11, pp. 3074–3088, 2023.
- [18] F. Mkaem and S. Boumaiza, “Physically inspired neural network model for RF power amplifier behavioral modeling and digital predistortion,” *IEEE Transactions on Microwave Theory and Techniques*, vol. 59, no. 4, pp. 913–923, 2011.
- [19] A. Faraji, S. A. Sadrossadat, W. Na, F. Feng, and Q.-J. Zhang, “A new macromodeling method based on deep gated recurrent unit regularized with gaussian dropout for nonlinear circuits,” *IEEE Transactions on Circuits and Systems I (TCAS I)*, vol. 70, no. 7, pp. 2904–2915, 2023.
- [20] S. Zebhi, S. A. Sadrossadat, W. Na, and Q.-J. Zhang, “Macromodeling of nonlinear high-speed circuits using novel hybrid bidirectional high-order deep recurrent neural network,” *IEEE Transactions on Circuits and Systems I (TCAS I)*, vol. 71, no. 8, pp. 3740–3753, 2024.
- [21] Z. Hu, Y. Xiao, H. Wang, J. Yu, and Z. Gao, “Deep learning modeling method for RF devices based on uniform noise training set,” 2024.
- [22] S. Qi and C. D. Sarris, “Deep neural networks for rapid simulation of planar microwave circuits based on their layouts,” *IEEE Transactions on Microwave Theory and Techniques*, vol. 70, no. 11, pp. 4805–4815, 2022.
- [23] R. Shibata, M. Ohira, and Z. Ma, “A novel convolutional-autoencoder based surrogate model for fast s-parameter calculation of planar bpf,” in *IEEE/MTT-S International Microwave Symposium (IMS)*, 2022, pp. 498–501.
- [24] H. M. Torun, H. Yu, N. Dasari, V. C. K. Chekuri, A. Singh, J. Kim, S. K. Lim, S. Mukhopadhyay, and M. Swaminathan, “A spectral convolutional net for co-optimization of integrated voltage regulators and embedded inductors,” in *IEEE/ACM International Conference on Computer-Aided Design (ICCAD)*, 2019, pp. 1–8.
- [25] H. M. Torun, A. C. Durgun, K. Aygün, and M. Swaminathan, “Causal and passive parameterization of S-parameters using neural networks,” *IEEE Transactions on Microwave Theory and Techniques*, vol. 68, no. 10, pp. 4290–4304, 2020.
- [26] H. Chae, H. Yu, S. Li, and D. Z. Pan, “PulseRF: Physics augmented ml modeling and synthesis for high-frequency RFIC design,” in *Proceedings of the IEEE/ACM International Conference on Computer-Aided Design*, ser. ICCAD ’24, 2025.
- [27] J. Zhou, E. A. Karahan, S. Ghoszy, Z. Liu, H. Jalili, and K. Sengupta, “25.3 AI-enabled design space discovery and end-to-end synthesis for RFICs with reinforcement learning and inverse methods demonstrating mm-Wave/sub-THz PAs between 30 and 120GHz,” in *IEEE International Solid-State Circuits Conference (ISSCC)*, vol. 68, 2025, pp. 1–3.
- [28] M. Fayazi, M. T. Taba, A. Tabatabavakili, E. Afshari, and R. Dreslinski, “FuNToM: Functional modeling of RF circuits using a neural network assisted two-port analysis method,” in *Proceedings of the IEEE/ACM International Conference on Computer Aided Design (ICCAD)*, 2023, pp. 1–8.
- [29] G. Zhang, H. He, and D. Katabi, “Circuit-GNN: Graph neural networks for distributed circuit design,” in *Proceedings of the International Conference on Machine Learning (ICML)*, ser. Proceedings of Machine Learning Research, K. Chaudhuri and R. Salakhutdinov, Eds., vol. 97, 2019, pp. 7364–7373.
- [30] H. Wang, K. Wang, J. Yang, L. Shen, N. Sun, H.-S. Lee, and S. Han, “GCN-RL circuit designer: Transferable transistor sizing with graph neural networks and reinforcement learning,” in *ACM/IEEE Design Automation Conference (DAC)*, 2020, pp. 1–6.
- [31] G. Li, C. Xiong, A. Thabet, and B. Ghanem, “DeeperGCN: All you need to train deeper GCNs,” 2020.
- [32] K. Hakhamaneshi, M. Nassar, M. Phielipp, P. Abbeel, and V. Stojanovic, “Pretraining graph neural networks for few-shot analog circuit modeling and design,” *IEEE Transactions on Computer-Aided Design of Integrated Circuits and Systems (TCAD)*, vol. 42, no. 7, pp. 2163–2173, 2023.
- [33] Z. Wu and I. Savidis, “Transfer of performance models across analog circuit topologies with graph neural networks,” in *Proceedings of the ACM/IEEE Workshop on Machine Learning for CAD (MLCAD)*, ser. MLCAD ’22, 2022, p. 159–165.
- [34] Z. Wu and I. Savidis, “Transfer learning for reuse of analog circuit sizing models across technology nodes,” in *2022 IEEE International Symposium on Circuits and Systems (ISCAS)*, 2022, pp. 1033–1037.
- [35] H. Zhou, Y. Li, X. Xiong, and P. Zhou, “A transferable GNN-based multi-corner performance variability modeling for analog ICs,” in *Asia and South Pacific Design Automation Conference (ASP-DAC)*, 2024, pp. 411–416.
- [36] H. Ren, G. F. Kokai, W. J. Turner, and T.-S. Ku, “ParaGraph: Layout parasitics and device parameter prediction using graph neural networks,” in *Proceedings of the IEEE/ACM Design Automation Conference (DAC)*, 2020, pp. 1–6.
- [37] L. Liu, F. Yang, L. Shang, and X. Zeng, “GNN-Cap: Chip-scale interconnect capacitance extraction using graph neural network,” *IEEE Transactions on Computer-Aided Design of Integrated Circuits and Systems (TCAD)*, vol. 43, no. 4, pp. 1206–1217, 2024.
- [38] M. Liu, W. J. Turner, G. F. Kokai, B. Khailany, D. Z. Pan, and H. Ren, “Parasitic-aware analog circuit sizing with graph neural networks and Bayesian optimization,” in *Proceedings of the Design, Automation & Test in Europe Conference & Exhibition (DATE)*, 2021, pp. 1372–1377.
- [39] A. Mehradfar, X. Zhao, Y. Huang, E. Ceyani, Y. Yang, S. Han, H. Aghasi, and S. Avestimehr, “FALCON: An ML framework for fully automated layout-constrained analog circuit design,” 2025.
- [40] K. Kunal, T. Dhar, M. Madhusudan, J. Poojary, A. Sharma, W. Xu, S. M. Burns, J. Hu, R. Harjani, and S. S. Sapatnekar, “GANA: Graph convolutional network based automated netlist annotation for analog circuits,” in *Design, Automation & Test in Europe Conference & Exhibition (DATE)*, 2020, pp. 55–60.
- [41] M. Fayazi, M. T. Taba, E. Afshari, and R. Dreslinski, “AnGeL: Fully-automated analog circuit generator using a neural network assisted semi-supervised learning approach,” *IEEE Transactions on Circuits and Systems I (TCAS I)*, vol. 70, no. 11, pp. 4516–4529, 2023.
- [42] C. Li, D. Hu, and X. Zhang, “Pre-layout parasitic-aware design optimizing for RF circuits using graph neural network,” *Electronics*, vol. 12, no. 2, 2023.
- [43] K. Zhu, H. Chen, W. J. Turner, G. F. Kokai, P.-H. Wei, D. Z. Pan, and H. Ren, “TAG: Learning circuit spatial embedding from layouts,” in *Proceedings of the IEEE/ACM International Conference on Computer-Aided Design (ICCAD)*, 2022.
- [44] Z. Wu, S. Pan, F. Chen, G. Long, C. Zhang, and P. S. Yu, “A comprehensive survey on graph neural networks,” *IEEE Transactions on Neural Networks and Learning Systems (NeurIPS)*, vol. 32, no. 1, pp. 4–24, 2021.
- [45] D. Utyamishv and I. Partin-Vaisband, “Netwise detection of hardware trojans using scalable convolution of graph embedding clouds,” *IEEE Transactions on Computer-Aided Design of Integrated Circuits and Systems (TCAD)*, vol. 43, no. 10, pp. 3116–3128, 2024.
- [46] T. Mohamed, V. M. van Santen, L. Alrahis, O. Sinanoglu, and H. Amrouch, “Graph attention networks to identify the impact of transistor degradation on circuit reliability,” *IEEE Transactions on Circuits and Systems I (TCAS I)*, vol. 71, no. 7, pp. 3269–3281, 2024.
- [47] G. Papamakarios, T. Pavlakou, and I. Murray, “Masked autoregressive flow for density estimation,” in *Advances in Neural Information Processing Systems (NeurIPS)*, I. Guyon, U. V. Luxburg, S. Bengio, H. Wallach, R. Fergus, S. Vishwanathan, and R. Garnett, Eds., vol. 30. Curran Associates, Inc., 2017.
- [48] C.-W. Huang, D. Krueger, A. Lacoste, and A. Courville, “Neural autoregressive flows,” in *Proceedings of the International Conference on Machine Learning (ICML)*, 10–15 Jul 2018, pp. 2078–2087.
- [49] G. Papamakarios, E. Nalisnick, D. J. Rezende, S. Mohamed, and B. Lakshminarayanan, “Normalizing flows for probabilistic modeling and inference,” *Journal of Machine Learning Research*, vol. 22, no. 57, pp. 1–64, 2021.
- [50] M. Fey and J. E. Lenssen, “Fast graph representation learning with PyTorch Geometric,” in *ICLR Workshop on Representation Learning on Graphs and Manifolds*, 2019.
- [51] C. Durkan, A. Bekasov, I. Murray, and G. Papamakarios, “inflows: normalizing flows in PyTorch,” Nov. 2020. [Online]. Available: <https://doi.org/10.5281/zenodo.4296287>